The librational ground state of monodeuteromethane adsorbed on the surface of graphite

P. C. Ball, A. Inaba, J. A. Morrison, M. V. Smalley, and R. K. Thomas

---

Articles you may be interested in

Vacuum ultraviolet surface photochemistry of water adsorbed on graphite
J. Chem. Phys. 117, 6667 (2002); 10.1063/1.1506143

The librational ground state of monodeuterated methane adsorbed on graphite
J. Chem. Phys. 103, 1627 (1995); 10.1063/1.469734

Scanning tunneling microscopy theory for an adsorbate: Application to adenine adsorbed on a graphite surface
J. Chem. Phys. 100, 7814 (1994); 10.1063/1.466824

Splittings of the librational ground state of CH3D physisorbed on the surface of graphite
J. Chem. Phys. 74, 2049 (1981); 10.1063/1.441250

Argon Adsorbed on a Graphitic Surface. The Heat of Adsorption from Lattice Liquid Theory
J. Chem. Phys. 27, 1341 (1957); 10.1063/1.1744004

The librational ground state of monodeuteromethane adsorbed on the surface of graphite

P. C. Ball
Physical Chemistry Laboratory, University of Oxford, Oxford, OX1 3QZ, United Kingdom

A. Inaba
Department of Chemistry, Osaka University, Toyonaka, Osaka 560, Japan

J. A. Morrison[a]
Department of Chemistry, McMaster University, Hamilton, Ontario L8S 4M1, Canada

M. V. Smalley and R. K. Thomas[b]
Physical Chemistry Laboratory, University of Oxford, Oxford, OX1 3Q2, United Kingdom

The heat capacity of CH_3D on graphite has been measured at low temperatures (0.3–7 K) and shown to have a Schottky anomaly resulting from the difference in energy between states with the single deuterium atom pointing away from the surface (D up) and states where the deuterium atom is part of the tripod of atoms pointing towards the surface (D down). The energy difference is $380 \pm 20 \mu$eV with the D-down configuration being the more stable. Incoherent neutron scattering spectra of CH_3D adsorbed on exfoliated graphite have been used to resolve the finer detail of the tunneling splittings in the system. The energy levels can be described quantitatively in terms of five parameters, the splitting between D-up and D-down configurations and two pairs of parameters, one pair related to the rotational potential about the unique C–H(D) bond normal to the surface and the other pair to rotation about one of the three equivalent C–H(D) bonds pointing towards the surface. Comparison of the results from CH_3D and earlier results from CH_4 show that both potentials contain two Fourier components, approximately 75% of a threefold and 25% of a sixfold component in phase with one another. The values originally obtained from the CH_4 tunneling spectrum for the two barrier heights 202 and 172 cm^{-1} for rotation about the unique and nonunique axes, respectively, are shown to have an uncertainty of about 5% resulting from the approximations used for the shape of the potential in the interpretation of the earlier experiment.

I. INTRODUCTION

Methane on graphite is in many ways a model system for the study of physisorption. It has been well studied theoretically,[1-3] thermodynamically,[4-6] by diffraction,[7,8] and by neutron inelastic scattering.[9,10] The van der Waals diameter of the methane molecule is slightly smaller than the commensurate (C) $\sqrt{3} \times \sqrt{3}$ R 30° structure normally adopted by small molecules on graphite. At coverages well below a monolayer, methane adopts the C structure, but as the monolayer nears completion it undergoes a transition to an incommensurate structure. The rotational tunneling spectrum of CH_4 in its C phase on graphite has been analyzed to give quantitative information about the reorientational potential of the molecule.[10] In a tetrahedral potential, there are three librational energy levels, A, T, and E, but in the trigonal field of the surface and surrounding molecules the degeneracy of the T level is split to give a total of four levels. Five transitions occur in the incoherent neutron scattering spectrum, all of which have been observed. The spectrum has been quantitatively explained in terms of just two parameters, which are related to the heights of the barriers to rotation

about the unique C–H bond normal to the surface and about one of the three equivalent C–H bonds pointing towards the surface. The values of the barrier heights were found to be 202 and 172 cm^{-1}, respectively. A high precision was quoted for the values of these barrier heights because the tunneling splitting is extremely sensitive to small changes in the barrier. However, the precision is limited by the validity of the assumption that the potential for rotation about any one of the C–H bonds consists of a single Fourier component. The only way to test this assumption is to find out to what extent the rotational potential determined for CH_4 can be transferred to one of its isotopic derivatives. This however, is not an easy test to make. The first difficulty is that the lower symmetry of CH_3D, CH_2D_2, and CHD_3 greatly increases the complexity of the tunneling spectra. Secondly, the larger moment of inertia causes a substantial decrease in the tunneling frequencies, making it more difficult to resolve the splittings. Finally, the much lower incoherent scattering cross section of deuterium compared with hydrogen lowers the intensity of the transitions relative to an already high background scattering from the graphite. The combination of these factors makes CH_3D the only isotopic species feasible for further quantitative study.

There have been two previous studies of CH_3D on graphite. In a theoretical study, Maki[11] calculated the low-temperature heat capacity to be expected for CH_3D on

---

[a] Deceased October 20, 1987.
[b] Physical Chemistry Laboratory, South Parks Road, Oxford, OX1 3QZ, United Kingdom.

graphite; Inaba and Morrison[12] found that some of Maki's predictions were borne out by experiment, but their experiments were limited to the relaxation times for thermal equilibrium as a function of temperature. Maki also predicted the neutron scattering spectrum, but made errors in his analysis which lead to incorrect energies for four out of the seven possible states. He compared his predictions with an unpublished spectrum obtained by Smalley et al. for CH_3D adsorbed on an unoriented graphite Vulcan III. The difficulties of resolving the different lines are exacerbated on a powdered material because all transitions are observed regardless of their polarization with respect to the surface. This made any definite assignment of the spectrum impossible. Furthermore, there are small shifts in the energy levels between the different graphites and it may not be valid to compare matrix elements for the graphitized material with values deduced from exfoliated graphite. In this paper, we present a more thorough theoretical analysis of the problem, together with complete data for the heat capacity curves at two coverages and inelastic neutron scattering spectra from CH_3D on a partially oriented graphite. We begin with the theoretical analysis.

II. ENERGY LEVELS OF CH₃D ON GRAPHITE

The spectrum of CH_4 on graphite was analyzed quantitatively using the pocket state formalism of Huller[10,13] and we adapt this method to the present problem. The functional space is restricted to the 12 localized wave functions (pocket states) that correspond to the 12 equilibrium orientations of the molecule in the field. For CH_3D on the surface of graphite, these orientations are shown in Fig. 1, which also serves to introduce our labeling of the pocket states. There are two types of nonequivalent pocket states, those with the D atom pointing away from the surface (ϕ_1, ϕ_5, and ϕ_9, henceforth called the D-up states) and those with D pointing towards the surface (henceforth called the D-down states).
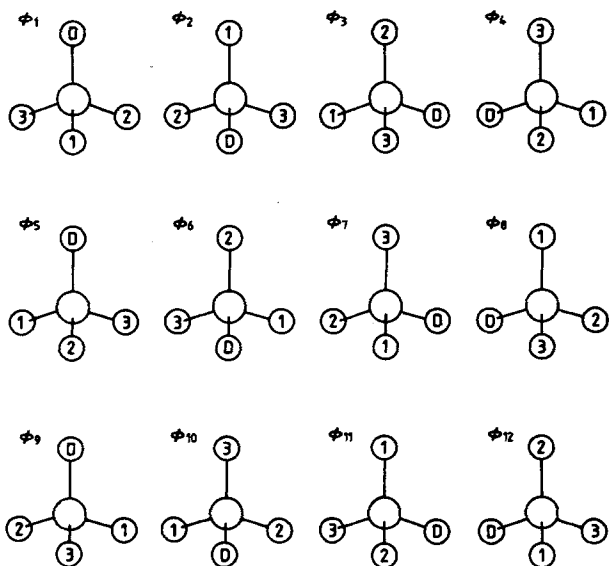
The rotational Hamiltonian matrix is obtained as follows: Consider first the possible threefold rotations (Fig. 2). The rotational axes are denoted by $C_3^u(H), C_3^u(D), C_3^d(H)$, and $C_3^d(D)$, where u denotes the axis perpendicular to the surface, d denotes an axis at the tetrahedral angle $\tan^{-1}\sqrt{8}$ from the perpendicular axis, and (H) and (D) indicate whether the axis lies along to a C–H or a C–D bond, respectively. For ϕ_1, there are two nonequivalent threefold axes $C_3^u(D)$ and $C_3^d(H)$, and the states produced by rotation about these axes are

$$\phi_1 \xrightarrow{C_3^u(D)} \phi_5,\phi_9 \text{ (both D-up states)},$$

$$\phi_1 \xrightarrow{C_3^d(H)} \phi_8,\phi_{10} \text{ (both D-down states)}.$$

Two types of matrix elements in the rotational Hamiltonian matrix arise from these rotations and are defined by

$$\langle\phi_1|H|\phi_5\rangle = H_{15} = h_4, \qquad (2.1)$$

$$\langle\phi_1|H|\phi_8\rangle = H_{18} = h_2. \qquad (2.2)$$

As far as possible, we use the same notation as Smalley et al.[10] and Maki,[11] but, as will be explained below, our h_2 is different from Maki's notation for the matrix element (2.2). We now consider one of the D-down states as the starting orientation, taking ϕ_2 as an example. There are three nonequivalent threefold axes for this pocket state—$C_3^u(H)$, $C_3^d(H)$, and $C_3^d(D)$. The states produced by rotation about these axes are

$$\phi_2 \rightarrow \phi_8,\phi_{11} \text{ (both D-down states)}, \quad C_3^u(H),$$

$$\phi_2 \rightarrow \phi_6,\phi_{10} \text{ (both D-down states)}, \quad C_3^d(D),$$

$$\phi_2 \rightarrow \phi_5,\phi_{12}, \quad C_3^d(H).$$

For the last case, rotation by 120° about the $C_3^d(H)$ axis in one direction gives the D-up state ϕ_5, whereas rotation in the other direction gives the D-down state ϕ_{12}. Thus there are two distinct types of matrix element arising from the rotations about this one axis. This is where the earlier analysis by Maki[12] is incorrect: he assumes that both forward and backward rotations about this axis result in the same matrix element. This evidently cannot be the case, since one rotation interconverts equivalent states, while the other interconverts
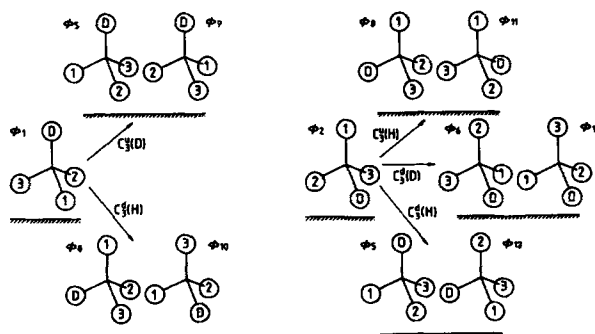

FIG. 1. The 12 equilibrium orientations of CH_3D on the surface of graphite with the corresponding pocket states.

FIG. 2. The threefold rotations of CH_3D in a trigonal field.

TABLE I. The Hamiltonian matrix for the pocket states $|\phi_i\rangle$.

a_4	H	H	H	h_4	h_2	h_2	h_2	h_4	h_2	h_2	h_2
H	a	H	H	h_2	h	f	f_4	h_2	h	f_4	f
H	H	a	H	h_2	f_4	h	f	h_2	f	h	f_4
H	H	H	a	h_2	f	f_4	h	h_2	f_4	f	h
h_4	h_2	h_2	h_2	a_4	H	H	H	h_4	h_2	h_2	h_2
h_2	h	f_4	f	H	a	H	H	h_2	h	f	f_4
h_2	f	h	f_4	H	H	a	H	h_2	f	f_4	f
h_2	f_4	f	h	H	H	H	a	h_2	f	f_4	h
h_4	h_2	h_2	h_2	h_4	h_2	h_2	h_2	a_4	H	H	H
h_2	h	f	f_4	h_2	h	f_4	f	H	a	H	H
h_2	f_4	h	f	h_2	f	h	f_4	H	H	a	H
h_2	f	f_4	h	h_2	f_4	f	h	H	H	H	a

nonequivalent states. The $\phi_2 \rightarrow \phi_5$ rotation is in fact equivalent to the $\phi_1 \rightarrow \phi_8$ rotation, so from Eq. (2.2) we have

$$\langle \phi_2 | H | \phi_5 \rangle = h_2.$$

The remaining three matrix elements arising from the rotations of ϕ_2 are defined as follows:

$$\langle \phi_2 | H | \phi_8 \rangle = f_4, \tag{2.3}$$

$$\langle \phi_2 | H | \phi_6 \rangle = h, \tag{2.4}$$

$$\langle \phi_2 | H | \phi_{12} \rangle = f. \tag{2.5}$$

There are thus five distinct off-diagonal threefold elements in the Hamiltonian, of which h_2 is the only one between nonequivalent pocket states.

The diagonal elements of the Hamiltonian matrix are the pocket state energies. There are two such elements, defined by

$$\langle \phi_1 | H | \phi_1 \rangle = a_4, \tag{2.6}$$

$$\langle \phi_2 | H | \phi_2 \rangle = a. \tag{2.7}$$

We also follow Maki by setting all twofold overlap matrix elements, H in Table I, to zero, an approximation that can be

well justified.[10,14] The whole 12×12 matrix can then be constructed by inspection of Fig. 1 and is shown in Table I.

It is straightforward to diagonalize this matrix using the group theory described by Smalley and Ball.[15] For convenience we reproduce in Table II the character table for the group $(C_{3v}, \overline{C}_{3v})$ appropriate to the problem. The meaning of the permutation operations (123), etc., is described fully by Smalley and Ball.[15] The pocket states produced by operating on the two example functions ϕ_1 and ϕ_2 with such operations are given in the central part of the table and the representation Γ_ϕ based upon the 12 pocket states is given in the lower part. This representation reduces to

$$\Gamma_\phi = 2A_1 + E_1 + E_2 + 2E_3 + E_4.$$

The eigenfunctions of the problem are found by applying projection operators of each symmetry type to the two example functions and are given in Table III. Like the pocket state wave functions themselves, the eigenfunctions separate into two types, two containing only the D-up states and the other five only the D-down states. The distinction between these two types of eigenfunction with the same symmetry is made with the superscripts (u) and (d).

The derivation of the eigenenergies given on the right-hand side of Table III is trivial. However, there may be mixing between the two states of A_1 symmetry and between the two states of E_3 symmetry. The extent of this mixing depends on the matrix element between the interacting states, which is simply a multiple of h_2 in both cases. h_2 is the matrix element between D-up and D-down states and is therefore absent from Table III. The tunneling between nonequivalent sites is expected to be orders of magnitude smaller than that between equivalent sites. Although this has not been shown explicitly for a threefold rotation, the problem of a bound particle tunneling between two potential wells with different energy minima has been extensively studied.[16,17] A review of these calculations[18] concluded that the tunneling splitting

TABLE II. Character table for the group $G = (C_{3v}, \overline{C}_{3v})$.

$(C_{3v}, \overline{C}_{3v})$	$E\overline{E}$	$2E$ $(\overline{123})$	$2(123)$ $\overline{E}$	$2(123)$ $(\overline{123})$	$2(123)$ $(\overline{132})$	$9(12)*$ $(\overline{12})*$
A_1	1	1	1	1	1	1
A_2	1	1	1	1	1	1
E_1	2	-1	2	-1	-1	0
E_2	2	2	-1	-1	-1	0
E_3	2	-1	-1	2	-1	0
E_4	2	-1	-1	-1	2	0

	$E\overline{E}$	$2E(\overline{123})$	$2(123)\overline{E}$	$2(123)(\overline{123})$	$2(123)(\overline{132})$	$9(12)*(\overline{12})*$
ϕ_1	ϕ_1	$\phi_5 + \phi_9$	$\phi_5 + \phi_9$	$2\phi_1$	$\phi_5 + \phi_9$	$3(\phi_1 + \phi_5 + \phi_9)$
ϕ_2	ϕ_2	$\phi_6 + \phi_{10}$	$\phi_8 + \phi_{11}$	$\phi_3 + \phi_4$	$\phi_7 + \phi_{12}$	$\phi_2 + \phi_3 + \phi_4 + \phi_6$ $+ \phi_7 + \phi_8 + \phi_{10} + \phi_{11} + \phi_{12}$
Γ_ϕ	12	0	0	3	0	2

	EE	$2E$ $(\overline{123})$	$2(123)$ $\overline{E}$	$2(123)$ $(\overline{123})$	$2(123)$ $(\overline{132})$	$9(12)*$ $(\overline{12})*$
Γ_χ	32	8	2	8	2	8

TABLE III. The seven symmetry adapted eigenfunctions for CH_3D on graphite and the corresponding eigenenergies.

$$\psi_{A_1}^{(u)} = \frac{1}{\sqrt{3}}(\phi_1 + \phi_5 + \phi_9) \qquad E_{A_1}^{(u)} = a_4 + 2h_4$$

$$\psi_{A_1}^{(d)} = \frac{1}{3}(\phi_2 + \phi_3 + \phi_4 + \phi_5 + \phi_6 + \phi_7 + \phi_8 + \phi_{10} + \phi_{11} + \phi_{12}) \qquad E_{A_1}^{(d)} = a + 2f_4 + 2h + 2f$$

$$\psi_{E_1}^{(u)} = \frac{1}{\sqrt{6}}(2\phi_1 - \phi_5 - \phi_9) \qquad E_{E_1}^{(u)} = a_4 - h_4$$

$$\psi_{E_1}^{(d)} = \frac{1}{3\sqrt{2}}(2\phi_2 + 2\phi_3 + 2\phi_4 - \phi_6 - \phi_7 - \phi_8 - \phi_{10} - \phi_{11} - \phi_{12}) \qquad E_{E_1}^{(d)} = a - f_4 - h - f$$

$$\psi_{E_1} = \frac{1}{3\sqrt{2}}(2\phi_2 - \phi_3 - \phi_4 + 2\phi_8 - \phi_6 - \phi_7 + 2\phi_{11} - \phi_{10} - \phi_{12}) \qquad E_{E_1} = a + 2f_4 - h - f$$

$$\psi_{E_2} = \frac{1}{3\sqrt{2}}(2\phi_2 - \phi_3 - \phi_4 + 2\phi_6 - \phi_7 - \phi_8 + 2\phi_{10} - \phi_{11} - \phi_{12}) \qquad E_{E_2} = a - f_4 + 2h - f$$

$$\psi_{E_4} = \frac{1}{3\sqrt{2}}(2\phi_2 - \phi_3 - \phi_4 + 2\phi_7 - \phi_6 - \phi_8 + 2\phi_{12} - \phi_{10} - \phi_{11}) \qquad E_{E_4} = a - f_4 - h + 2f$$

decreases rapidly when asymmetry, however small, is introduced into the potential. We have adapted a formula for this effect from Harmony[18] to estimate the perturbation to the A_1 and E_3 levels of Table III is of the order of $10^{-7} \mu$eV (see the Appendix), entirely negligible compared with the symmetrical threefold overlaps (see below).

The expressions for the eigenenergies in Table III are different from those derived by Maki, who took h_2 and f to be equal. This overestimates the magnitude of the perturbation between upper and lower states, giving an incorrect square root term in his Eqs. (2.1) and (2.5), which is absent from our work.

III. INTENSITIES OF THE TUNNELING TRANSITIONS

Maki calculated the intensities of the tunneling transitions in the incoherent neutron scattering spectrum, but only for one value of κ (the momentum transfer), which unfortunately does not correspond to the range of our experiments. Here we give fuller account of the application of the pocket-state formalism to the three-proton problem and calculate the intensities of the lines as a function of κ.

Since incoherent neutron scattering changes the nuclear spin wave function, though not necessarily the overall nuclear spin, of the molecule, it is necessary to consider the full wave function in order to calculate the intensities of the different transitions in the tunneling spectrum. Smalley *et al.*[10] have analyzed this problem for CH_4 on graphite and their treatment is extended here to CH_3D on graphite.

There is no coupling of the spins to the rotational motion because the Hamiltonian does not depend on the spin coordinates. Pocket-state wave functions $|\chi_m\rangle$ may therefore be constructed from products of the 12 pocket state wave functions $|\phi_i\rangle$, the eight nuclear spin wave functions of the three protons $|\mu_1\mu_2\mu_3\rangle$ and the three nuclear spin wave functions of the deuteron $|\mu_D\rangle$. These 96 wave functions can be arranged in 32 groups of three, the three arising from degeneracy of the spin wave function of the deuteron. The 32 wave functions have the form

$$\chi_m\rangle = \sum_m |\phi_1\rangle|\mu_1\mu_2\mu_3\mu_D\rangle$$

where m is an index selecting the components that combine

to satisfy the overall symmetry requirements. Whereas the pocket-state wave functions $|\phi_i\rangle$ correspond to a particular configuration of the labeled protons (Fig. 1), the symmetrized functions $|\chi_m\rangle$ correspond to a particular configuration of spins at labeled sites and are not eigenfunctions of the system. The 32 $|\chi_m\rangle$ are drawn in Fig. 3, the configurations
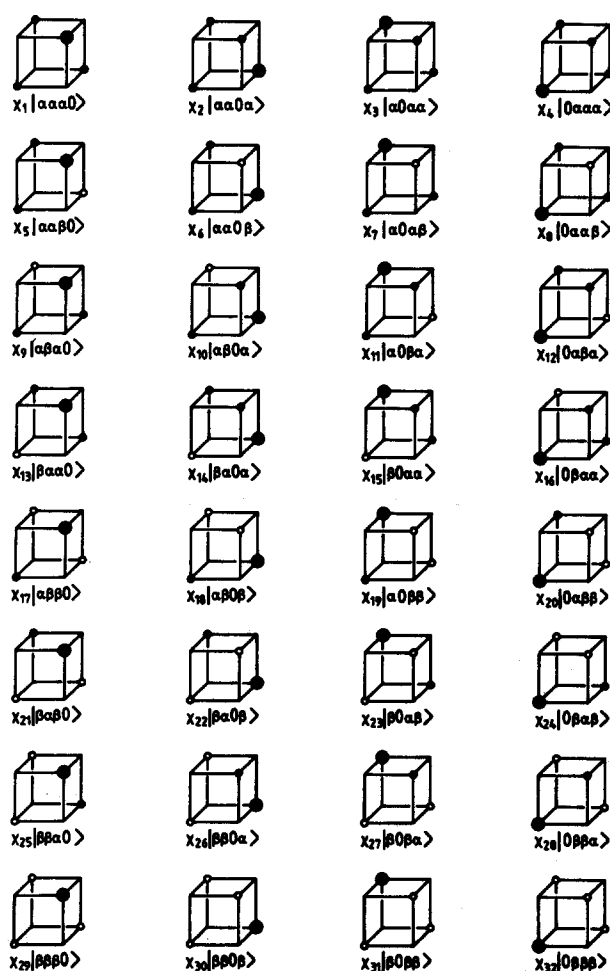

FIG. 3. The 32 totally symmetric wave functions $|\mu_1\mu_2\mu_3\mu_D\rangle$ which define the spin states at the four particle positions in the reference system of the crystal field. The left-hand column represents the wave functions with the C–D bond pointing away from the surface.

TABLE IV. The 32 symmetry adapted wave functions $|\psi_\alpha\rangle$ for CH_3D in a trigonal field.

$$\psi^1_{A_1} = \chi_1 \quad \psi^2_{A_1} = 1/\sqrt{3}(\chi_5 + \chi_9 + \chi_{13}) \quad \psi^3_{A_1} = \frac{1}{\sqrt{3}}(\chi_{17} + \chi_{21} + \chi_{25})$$

$$\psi^4_{A_1} = \chi_{29} \quad \psi^5_{A_1} = \frac{1}{\sqrt{3}}(\chi_2 + \chi_3 + \chi_4)$$

$$\psi^6_{A_1} = \frac{1}{3}(\chi_6 + \chi_7 + \chi_8 + \chi_{10} + \chi_{11} + \chi_{12} + \chi_{14} + \chi_{15} + \chi_{16})$$

$$\psi^7_{A_1} = \frac{1}{3}(\chi_{18} + \chi_{19} + \chi_{20} + \chi_{22} + \chi_{23} + \chi_{24} + \chi_{26} + \chi_{27} + \chi_{28})$$

$$\psi^8_{A_1} = \frac{1}{\sqrt{3}}(\chi_{30} + \chi_{31} + \chi_{32})$$

$$\psi^1_{E_1} = \frac{1}{3\sqrt{2}}(2\chi_6 + 2\chi_7 + 2\chi_8 - \chi_{10} - \chi_{11} - \chi_{12} - \chi_{14} - \chi_{15} - \chi_{16})$$

$$\psi^2_{E_1} = \frac{1}{\sqrt{6}}(\chi_{10} + \chi_{12} + \chi_{15} - \chi_{11} - \chi_{14} - \chi_{16})$$

$$\psi^3_{E_1} = \frac{1}{3\sqrt{2}}(2\chi_{26} + 2\chi_{27} + 2\chi_{28} - \chi_{18} - \chi_{19} - \chi_{20} - \chi_{22} - \chi_{23} - \chi_{24})$$

$$\psi^4_{E_1} = \frac{1}{\sqrt{6}}(\chi_{22} + \chi_{19} + \chi_{24} - \chi_{18} - \chi_{20} - \chi_{23})$$

$$\psi^1_{E_2} = \frac{1}{\sqrt{6}}(2\chi_2 - \chi_3 - \chi_4) \quad \psi^2_{E_2} = \frac{1}{\sqrt{2}}(\chi_3 - \chi_4)$$

$$\psi^3_{E_2} = \frac{1}{3\sqrt{2}}(2\chi_6 + 2\chi_{10} + 2\chi_{14} - \chi_7 - \chi_8 - \chi_{11} - \chi_{12} - \chi_{15} - \chi_{16})$$

$$\psi^4_{E_2} = \frac{1}{\sqrt{6}}(\chi_7 + \chi_{11} + \chi_{15} - \chi_8 - \chi_{12} - \chi_{16})$$

$$\psi^5_{E_2} = \frac{1}{3\sqrt{2}}(2\chi_{26} + 2\chi_{18} + 2\chi_{22} - \chi_{19} - \chi_{20} - \chi_{23} - \chi_{24} - \chi_{27} - \chi_{28})$$

$$\psi^6_{E_2} = \frac{1}{\sqrt{6}}(\chi_{19} + \chi_{23} + \chi_{27} - \chi_{20} - \chi_{24} - \chi_{28}) \quad \psi^7_{E_2} = \frac{1}{\sqrt{6}}(2\chi_{30} - \chi_{31} - \chi_{32})$$

$$\psi^8_{E_2} = \frac{1}{\sqrt{2}}(\chi_{31} - \chi_{32})$$

$$\psi^1_{E_3} = \frac{1}{\sqrt{6}}(2\chi_5 - \chi_9 - \chi_{13}) \quad \psi^2_{E_3} = \frac{1}{\sqrt{2}}(\chi_9 - \chi_{13}) \quad \psi^3_{E_3} = \frac{1}{\sqrt{6}}(2\chi_{25} - \chi_{21} - \chi_{17})$$

$$\psi^4_{E_3} = \frac{1}{\sqrt{2}}(\chi_{21} - \chi_{17}) \quad \psi^5_{E_3} = \frac{1}{3\sqrt{2}}(2\chi_6 + 2\chi_{15} + 2\chi_{16} - \chi_7 - \chi_8 - \chi_{10} - \chi_{11} - \chi_{12} - \chi_{14})$$

$$\psi^6_{E_3} = \frac{1}{\sqrt{6}}(\chi_7 + \chi_{12} + \chi_{14} - \chi_8 - \chi_{10} - \chi_{11})$$

$$\psi^7_{E_3} = \frac{1}{3\sqrt{2}}(2\chi_{26} + 2\chi_{19} + 2\chi_{20} - \chi_{18} - \chi_{22} - \chi_{23} - \chi_{24} - \chi_{27} - \chi_{28})$$

$$\psi^8_{E_3} = \frac{1}{\sqrt{6}}(\chi_{27} + \chi_{24} + \chi_{18} - \chi_{22} - \chi_{23} - \chi_{28})$$

$$\psi^1_{E_4} = \frac{1}{3\sqrt{2}}(2\chi_6 + 2\chi_{11} + 2\chi_{12} - \chi_7 - \chi_8 - \chi_{10} - \chi_{14} - \chi_{15} - \chi_{16})$$

$$\psi^2_{E_4} = \frac{1}{\sqrt{6}}(\chi_{10} + \chi_7 + \chi_{16} - \chi_8 - \chi_{14} - \chi_{15})$$

$$\psi^3_{E_4} = \frac{1}{3\sqrt{2}}(2\chi_{26} + 2\chi_{23} + 2\chi_{24} - \chi_{18} - \chi_{19} - \chi_{20} - \chi_{22} - \chi_{27} - \chi_{28})$$

$$\psi^4_{E_4} = \frac{1}{\sqrt{6}}(\chi_{22} + \chi_{27} + \chi_{20} - \chi_{18} - \chi_{19} - \chi_{28})$$

in the first column representing the states with the deuteron pointing away from the surface.

We use the group theory developed by Smalley and Ball[15] to diagonalize the Hamiltonian matrix in $|\chi_m\rangle$. The 32-fold representation Γ_χ of the double group based on these states is given in the lowest part of Table II. It may be reduced to

$$\Gamma_\chi = 8A_1 + 2E_1 + 4E_2 + 4E_3 + 2E_4.$$

Application of the projection operators of these symmetries applied to the basis states projects out the 32 eigenfunctions $|\Psi_\alpha\rangle$ listed in Table IV. Alternatively, the correct eigenfunctions may be obtained by

$$|\Psi_\alpha\rangle = \sum_{m=1}^{32} b_{\alpha m}|\chi_m\rangle$$

where the matrix $b_{\alpha m}$ is given in Table V.

In incoherent scattering, only single molecule transitions are observed, although the scattering is coherent with respect to the protons in an individual molecule. The partial differential scattering cross section is

$$\frac{d^2\sigma}{d\Omega dE'} = N \sum_{\mu\mu'} \sum_{\alpha\alpha'} P_\mu P_\alpha |A_{\mu'\alpha'\mu\alpha}|^2 \delta(E - E'_{\alpha\alpha'})$$

where P_μ is the probability of occupation of the initial neutron spin state, P_α the probability of occupation of the initial state of the system, the δ function conserves energy, and $A_{\mu'\alpha'\mu\alpha}$ is the matrix element of the incoherent scattering amplitude operator

$$A_{\mu'\alpha'\mu\alpha} = \sum_{\gamma=1}^{4} \langle \mu'\Psi_{\alpha'} |(b^\gamma - \bar{b})\exp(i\boldsymbol{\kappa}\cdot\mathbf{r}_\gamma)|\mu\psi_\alpha\rangle,$$

TABLE V. The unitary matrix b_{am} which transforms the states $|\chi_m\rangle$ into the eigenstates of the system. $a = 1/\sqrt{3}$, $b = 1/3$, $c = 2/3\sqrt{2}$, $d = -1/3\sqrt{2}$, $e = 1/\sqrt{6}$, $f = -1/\sqrt{6}$, $g = 2/\sqrt{6}$, $h = 1/\sqrt{2}$, and $j = -1/\sqrt{2}$.

```
1 0 0 0 0 0 0 0 0 0 0 0 0 0 0 0 0 0 0 0 0 0 0 0 0 0 0 0 0 0 0 0 0 0 0 0
0 0 0 0 a 0 0 0 a 0 0 0 a 0 0 0 0 0 0 0 0 0 0 0 0 0 0 0 0 0 0 0 0 0 0 0
0 0 0 0 0 0 0 0 0 0 0 0 0 0 a 0 0 0 a 0 0 0 a 0 0 0 0 0 0 0 0 0
0 0 0 0 0 0 0 0 0 0 0 0 0 0 0 0 0 0 0 0 0 0 0 0 0 0 0 0 1 0 0 0
0 a a a 0 0 0 0 0 0 0 0 0 0 0 0 0 0 0 0 0 0 0 0 0 0 0 0 0 0 0 0
0 0 0 0 0 b b b 0 b b b 0 b b b 0 0 0 0 0 0 0 0 0 0 0 0 0 0 0 0
0 0 0 0 0 0 0 0 0 0 0 0 0 0 0 0 b b b 0 b b b 0 b b b 0 0 0 0
0 0 0 0 0 0 0 0 0 0 0 0 0 0 0 0 0 0 0 0 0 0 0 0 a a a
0 0 0 0 0 c c c 0 d d d 0 d d d 0 0 0 0 0 0 0 0 0 0 0 0 0 0 0 0
0 0 0 0 0 0 0 0 e f e 0 f e f 0 0 0 0 0 0 0 0 0 0 0 0 0 0 0 0 0
0 0 0 0 0 0 0 0 0 0 0 0 0 0 0 d d d 0 d d d 0 c c c 0 0 0 0
0 0 0 0 0 0 0 0 0 0 0 0 0 0 0 0 f e f 0 e f e 0 0 0 0 0 0 0 0
0 g f f 0 0 0 0 0 0 0 0 0 0 0 0 0 0 0 0 0 0 0 0 0 0 0 0 0 0 0 0
0 0 h j 0 0 0 0 0 0 0 0 0 0 0 0 0 0 0 0 0 0 0 0 0 0 0 0 0 0 0 0
0 0 0 0 0 c d d 0 c d d 0 c d d 0 0 0 0 0 0 0 0 0 0 0 0 0 0 0 0
0 0 0 0 0 0 e f 0 0 e f 0 0 e f 0 0 0 0 0 0 0 0 0 0 0 0 0 0 0 0
0 0 0 0 0 0 0 0 0 0 0 0 0 0 0 0 c d d 0 c d d 0 c d d 0 0 0 0
0 0 0 0 0 0 0 0 0 0 0 0 0 0 0 0 e f 0 0 e f 0 0 e f 0 0 0 0
0 0 0 0 0 0 0 0 0 0 0 0 0 0 0 0 0 0 0 0 0 0 0 0 0 g f f
0 0 0 0 0 0 0 0 0 0 0 0 0 0 0 0 0 0 0 0 0 0 0 0 0 h j
0 0 0 0 g 0 0 0 f 0 0 0 f 0 0 0 0 0 0 0 0 0 0 0 0 0 0 0 0 0 0 0
0 0 0 0 0 0 0 0 h 0 0 0 j 0 0 0 0 0 0 0 0 0 0 0 0 0 0 0 0 0 0 0
0 0 0 0 0 0 0 0 0 0 0 0 0 0 f 0 0 0 f 0 0 0 g 0 0 0 0 0 0 0 0 0
0 0 0 0 0 0 0 0 0 0 0 0 0 0 j 0 0 0 h 0 0 0 0 0 0 0 0 0 0 0 0 0
0 0 0 0 0 c d d 0 d d d 0 d c c 0 0 0 0 0 0 0 0 0 0 0 0 0 0 0 0
0 0 0 0 0 0 e f 0 f f e 0 e 0 0 0 0 0 0 0 0 0 0 0 0 0 0 0 0 0 0
0 0 0 0 0 0 0 0 0 0 0 0 0 0 0 0 d c c 0 d d d 0 c d d 0 0 0 0
0 0 0 0 0 0 0 0 0 0 0 0 0 0 0 0 e 0 0 0 f f e 0 0 e f 0 0 0 0
0 0 0 0 0 c d d 0 d c c 0 d d d 0 0 0 0 0 0 0 0 0 0 0 0 0 0 0 0
0 0 0 0 0 0 e f 0 e 0 0 0 f f e 0 0 0 0 0 0 0 0 0 0 0 0 0 0 0 0
0 0 0 0 0 0 0 0 0 0 0 0 0 0 0 0 d d d 0 d c c 0 c d d 0 0 0 0
0 0 0 0 0 0 0 0 0 0 0 0 0 0 0 0 f f e 0 e 0 0 0 0 e f 0 0 0 0
```

TABLE VI. The scattering matrix $B^n_{m\mu,m\mu}$ between the states $|\chi_m\rangle$ in units of $2a_{inc}/\sqrt{3}$. The numbers 1–4 represent the respective scattering elements G_1 to G_4. The diagonal elements b_m, where m is the column number, are listed in Table VII. These diagonal elements are the non spin-flip elements $B_{m\mu,m\mu}$.

```
b 0 0 0 3 0 0 2 0 0 0 1 0 0 0 0 0 0 0 0 0 0 0 0 0 0 0 0 0 0 0 0 0 0 0 0
0 b 0 0 0 4 0 0 0 2 0 0 0 1 0 0 0 0 0 0 0 0 0 0 0 0 0 0 0 0 0 0 0 0 0 0
0 0 b 0 0 0 4 0 0 0 3 0 0 0 1 0 0 0 0 0 0 0 0 0 0 0 0 0 0 0 0 0 0 0 0 0
0 0 0 b 0 0 0 4 0 0 0 3 0 0 0 2 0 0 0 0 0 0 0 0 0 0 0 0 0 0 0 0 0 0 0 0
3 0 0 0 b 0 0 0 0 0 0 0 0 0 0 0 2 0 0 0 1 0 0 0 0 0 0 0 0 0 0 0 0 0 0 0
0 4 0 0 0 b 0 0 0 0 0 0 0 0 0 0 0 2 0 0 0 1 0 0 0 0 0 0 0 0 0 0 0 0 0 0
0 0 4 0 0 0 b 0 0 0 0 0 0 0 0 0 0 0 3 0 0 0 1 0 0 0 0 0 0 0 0 0 0 0 0 0
0 0 0 4 0 0 0 b 0 0 0 0 0 0 0 0 0 0 0 3 0 0 0 2 0 0 0 0 0 0 0 0 0 0 0 0
2 0 0 0 0 0 0 0 b 0 0 0 0 0 0 0 3 0 0 0 0 0 0 0 1 0 0 0 0 0 0 0 0 0 0 0
0 2 0 0 0 0 0 0 0 b 0 0 0 0 0 0 0 4 0 0 0 0 0 0 0 1 0 0 0 0 0 0 0 0 0 0
0 0 3 0 0 0 0 0 0 0 b 0 0 0 0 0 0 0 4 0 0 0 0 0 0 0 1 0 0 0 0 0 0 0 0 0
0 0 0 3 0 0 0 0 0 0 0 b 0 0 0 0 0 0 0 4 0 0 0 0 0 0 0 2 0 0 0 0 0 0 0 0
1 0 0 0 0 0 0 0 0 0 0 0 b 0 0 0 0 0 0 0 3 0 0 0 2 0 0 0 0 0 0 0 0 0 0 0
0 1 0 0 0 0 0 0 0 0 0 0 0 b 0 0 0 0 0 0 0 4 0 0 0 2 0 0 0 0 0 0 0 0 0 0
0 0 1 0 0 0 0 0 0 0 0 0 0 0 b 0 0 0 0 0 0 0 4 0 0 0 3 0 0 0 0 0 0 0 0 0
0 0 0 2 0 0 0 0 0 0 0 0 0 0 0 b 0 0 0 0 0 0 0 4 0 0 0 3 0 0 0 0 0 0 0 0
0 0 0 0 2 0 0 0 3 0 0 0 0 0 0 0 b 0 0 0 0 0 0 0 0 0 0 0 1 0 0 0 0 0 0 0
0 0 0 0 0 2 0 0 0 4 0 0 0 0 0 0 0 b 0 0 0 0 0 0 0 0 0 0 0 1 0 0 0 0 0 0
0 0 0 0 0 0 3 0 0 0 4 0 0 0 0 0 0 0 b 0 0 0 0 0 0 0 0 0 0 0 1 0 0 0 0 0
0 0 0 0 0 0 0 3 0 0 0 4 0 0 0 0 0 0 0 b 0 0 0 0 0 0 0 0 0 0 0 2
0 0 0 0 1 0 0 0 0 0 0 3 0 0 0 0 0 0 0 b 0 0 0 0 0 0 2 0 0 0
0 0 0 0 0 1 0 0 0 0 0 0 4 0 0 0 0 0 0 0 b 0 0 0 0 0 0 2 0 0
0 0 0 0 0 0 1 0 0 0 0 0 4 0 0 0 0 0 0 0 b 0 0 0 0 0 0 3 0
0 0 0 0 0 0 0 2 0 0 0 0 0 4 0 0 0 0 0 0 0 b 0 0 0 0 0 0 3
0 0 0 0 0 0 0 0 1 0 0 0 2 0 0 0 0 0 0 0 0 0 b 0 0 0 3 0 0 0
0 0 0 0 0 0 0 0 0 1 0 0 0 2 0 0 0 0 0 0 0 0 0 b 0 0 0 0 4 0 0
0 0 0 0 0 0 0 0 0 0 1 0 0 3 0 0 0 0 0 0 0 0 0 b 0 0 0 4 0
0 0 0 0 0 0 0 0 0 0 0 2 0 0 3 0 0 0 0 0 0 0 0 0 b 0 0 0 4
0 0 0 0 0 0 0 0 0 0 0 0 1 0 0 2 0 0 3 0 0 0 b 0 0 0
0 0 0 0 0 0 0 0 0 0 0 0 0 1 0 0 2 0 0 4 0 0 0 b 0 0
0 0 0 0 0 0 0 0 0 0 0 0 0 0 1 0 0 3 0 0 4 0 0 0 b 0
0 0 0 0 0 0 0 0 0 0 0 0 0 0 0 2 0 0 3 0 0 4 0 0 0 b
```

where γ is an index defining the four possible sites of the scattering proton, b^γ is the corresponding scattering length, and $\bar{b}$ the average scattering length. The matrix elements are more easily evaluated for the pocket-state wave functions. Thus,

$$A_{\mu'\alpha'\mu\alpha} = \sum_{mm'} b^*_{m'\alpha'} b_{m\alpha} B_{m\mu'm\mu},$$

where the $b_{m\alpha}$ matrices are as defined above and

$$B_{m'\mu'm\mu} = \sum_{\gamma=1}^{4} \langle\mu'|\langle\chi_{m'}|(b^\gamma - \bar{b})\exp(i\kappa\cdot r_\gamma)|\chi_m\rangle|\mu\rangle.$$

The spatial part of the matrix element $\langle\exp(i\kappa\cdot r_\gamma)\rangle$ is easily evaluated only if the pocket states are approximated by δ functions, in which case it becomes

$$G_\gamma = \exp(i\kappa\cdot r^0_\gamma),$$

where r^0_γ is the equilibrium position of the γth proton. The effect of this approximation, which has been discussed by Ozaki et al.,[19] is that we have ignored the form factor of the proton, which will be a reasonable assumption only if

$$\{\kappa(r^0_\gamma - r_\gamma)\}^2 \ll 1.$$

In the present set of experiments $\kappa \simeq 1-2$ Å^{-1} and $\{\kappa(r^0_\gamma - r_\gamma)\}^2$ will be less than 0.1 for librational amplitudes up to about 20° so that the condition is quite well fulfilled. The spin part of the matrix element is readily evaluated and the whole set of elements B is given in terms of G in Tables VI and VII.

Using the known transformation matrices b_{ma} the matrix elements A may then be evaluated and, taking P_μ to be 1/2 for an unpolarized neutron beam and calculating P_α from the parameters that fit the heat capacity data (see Sec. IV), the incoherent scattering cross sections of the different tunneling transitions may be expressed in terms of G.

The cross sections can be expanded to give two types of term

$$|G_i|^2 = 1$$

and

$$G_iG_j^* + G_i^*G_j = 2\cos\{\kappa(r_i - r_j)\}.$$

To be compared with the observed intensities, these must be averaged over all orientations about an axis perpendicular to the surface since only the normal to the surface is oriented with respect to the beam. The average yields two functions of κ:

$$t(\kappa) = \overline{\cos\{\kappa(r_i - r_j)\}}$$

and

$$f(\kappa) = \overline{\cos\{\kappa(r_i - r_4)\}},$$

where i and j are not equal to 4 and where the labels refer to

TABLE VII. Non-spin-flip scattering matrix elements $B_{m\mu,m\mu}$ for $\mu = \alpha$ and $\mu = \beta$. The units of these differ in sign: $B_{m\alpha,m\alpha} = b_m a_{inc}/\sqrt{3}$ and $B_{m\beta,m\beta} = -b_m a_{inc}/\sqrt{3}$.

m	b_m	m	b_m
1	$G_1 + G_2 + G_3$	17	$G_1 - G_2 - G_3$
2	$G_1 + G_2 + G_4$	18	$G_1 - G_2 - G_4$
3	$G_1 + G_3 + G_4$	19	$G_1 - G_3 - G_4$
4	$G_2 + G_3 + G_4$	20	$G_2 - G_3 - G_4$
5	$G_1 + G_2 - G_3$	21	$-G_1 + G_2 - G_3$
6	$G_1 + G_2 - G_4$	22	$-G_1 + G_2 - G_4$
7	$G_1 + G_3 - G_4$	23	$-G_1 + G_3 - G_4$
8	$G_2 + G_3 - G_4$	24	$-G_2 + G_3 - G_4$
9	$G_1 - G_2 + G_3$	25	$-G_1 - G_2 + G_3$
10	$G_1 - G_2 + G_4$	26	$-G_1 - G_2 + G_4$
11	$G_1 - G_3 + G_4$	27	$-G_1 - G_3 + G_4$
12	$G_2 - G_3 + G_4$	28	$-G_2 - G_3 + G_4$
13	$-G_1 + G_2 + G_3$	29	$-G_1 - G_2 - G_3$
14	$-G_1 + G_2 + G_4$	30	$-G_1 - G_2 - G_4$
15	$-G_1 + G_3 + G_4$	31	$-G_1 - G_3 - G_4$
16	$-G_2 + G_3 + G_4$	32	$-G_2 - G_3 - G_4$

the numbering of sites as in Fig. 4 of Smalley *et al.*[10] $t(\kappa)$ and $f(\kappa)$ may be evaluated for κ parallel and perpendicular to the surface to give

$$t(\kappa\perp), \quad f(\kappa_\perp) = \cos(4\kappa R/3),$$

$$t(\kappa\|) = J_0(\sqrt{\tfrac{8}{3}}\kappa R), \quad f(\kappa\|) = J_0(\sqrt{\tfrac{8}{3}}\kappa R),$$

where R is the C–H distance in CH_4 and $J_0(x)$ is the zeroth-order Bessel function of the first kind. The intensities of the transitions are expressed in terms of coefficients of t and f

$$I_{\alpha\alpha'} = n_{\alpha\alpha'}\left[(\text{const})_{\alpha\alpha'} + c_{\alpha\alpha'}t + c'_{\alpha\alpha'}f\right]$$

and the values of the three coefficients are given in Table VIII. The intensities are plotted as a function of κR in Fig. 4. Finally the spectra calculated for a value of κR equal to 1.6,

FIG. 4. Intensities of tunneling transitions for CH_3D on graphite as a function of κR. In (a) and (b), κ is parallel to the surface and the transitions have been divided into two for clarity. κ is perpendicular to the surface in (c). The value of κR for the spectra shown in Fig. 9 is arrowed.

TABLE VIII. Coefficients for the calculation of incoherent neutron scattering intensities for the transitions between rotational energy levels of CH_3D on graphite, in terms of the functions t and f. The units are $a^2_{inc}/1296$. Total scattering $= 3a^2_{inc} = 3888$.

Transition	Const.	$c_{\alpha\alpha'}$ (t)	$c'_{\alpha\alpha'}$ (f)
Elastic	1572	1164	1152
$A_1^{(u)}-E_3^{(u)}$	216	−216	0
$A_1^{(d)}-E_1$	96	48	−144
$A_1^{(d)}-E_2$	60	−60	0
$A_1^{(d)}-E_3^{(d)}$	24	−24	0
$A_1^{(d)}-E_4$	96	−96	0
E_1-E_2	120	−120	0
$E_1-E_3^{(d)}$	102	−102	0
E_1-E_4	30	−30	0
$E_2-E_3^{(d)}$	192	−48	−144
E_2-E_4	120	24	−144
$E_3^{(d)}-E_4$	102	42	−144
Total(u)	972	0	0
Total(d)	2916	0	0

corresponding approximately to the IN10 experiment to be described below, are drawn in Fig. 5. The positions of the lines in Fig. 5 have been obtained using the estimated values for the off-diagonal elements given by Maki[11] and the corrected expressions for the energy levels in Table III. The actual values of the energies are given in column 3 [energy (a)] of Table X. Maki used the calculations of Huller and Raich[14] to estimate the isotope effect on the overlap matrix elements and obtained $f = -4$ and $f_4 = -1.9 \mu eV$. h and h_4 for CH_4 are -14 and $-8 \mu eV$, respectively. The values obtained for the energy levels do not fit the experimental results.

IV. HEAT CAPACITY OF CH₃D ON GRAPHITE

A. Experimental details

The exfoliated graphite Grafoil MAT (Union Carbide) was used as an adsorbent. It had been heated in a chlorine atmosphere to 2000 °C to remove inorganic impurities and had specific surface area of 24 m^2 g^{-1} and a bulk density of 0.3 g cm^{-3}.[5] Strips of Grafoil to a total weight of 12.82 g
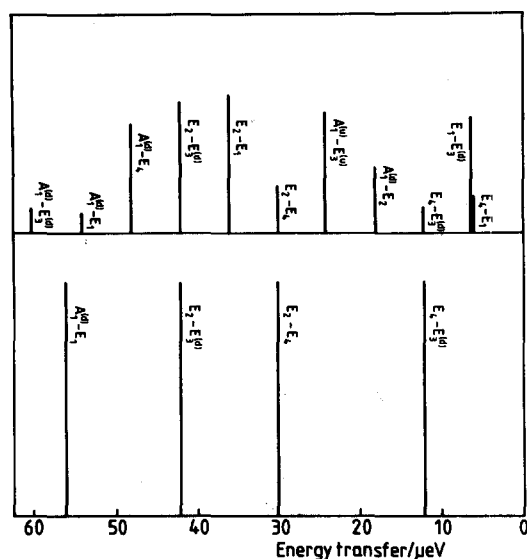
FIG. 5. Predicted neutron scattering spectrum for CH_3D on graphite, top κ parallel and bottom κ perpendicular to the surface. The $A\{^{(u)}_{(g)}\}-E\{^{(u)}_{(g)}\}$ transition has been given a Boltzmann weighting appropriate for the value of Δa determined in Sec. IV. The transition energies are those of column (A) in Table X.

were packed into the calorimeter vessel and the whole vessel outgassed at 2×10^{-4} Pa and 400 °C for two days. After cooling, the vessel was backfilled with helium gas and closed with an indium seal.

The preparation and analysis of CH_3D of high isotopic purity has been described elsewhere.[20] High-resolution mass spectra showed the specimen to contain 99.8 (+ 0.2, − 0.3)% CH_3D. Other impurities were estimated to be not more than 10 ppm.[20] The amount of gas introduced into the calorimeter vessel was measured volumetrically with an accuracy of about 0.2%. Before cooling the calorimeter with liquid helium the temperature was held at 80 K, where essentially all the gas introduced should be adsorbed on the graphite for a minimum of 15 h. It was then cooled slowly and held at 4.2 K while helium exchange gas was completely removed by pumping over another 15 h before measurements were begun. The amount of gas was measured before and after the heat capacity measurements and found to be the same within experimental accuracy.

One of the main experimental difficulties encountered in heat capacity measurements for such adsorbed systems is the long equilibrium time caused by poor thermal contact between the adsorbent and the calorimeter vessel. Despite the soft contact between the graphite and the vessel and the low bulk density of the Grafoil, we found unexpectedly that thermal equilibrium appeared to be established in the calorimeter vessel within seconds of the heating being switched off. This was of great advantage for investigating thermal relaxation effects of the adsorbed phase, which together with the calorimeter, are described elsewhere.[12]

B. Results

The heat capacity of two submonolayer samples with 3.014 and 2.590 mmol CH_3D was measured over the range

TABLE IX. Measured heat capacities of CH_3D on Grafoil MAT 12.82 g. Temperature (T) in K and heat capacity (C) in $J\,K^{-1}\,mol^{-1}$. Values quoted in order of measurement. (a) 3.014 mmol CH_3D ($\theta = 0.94$). (b) 2.590 mmol CH_3D ($\theta = 0.81$).

	T	C	T	C	T	C
(a)	0.283	4.458	2.512	1.534	3.353	1.330
	0.309	4.010	2.730	1.486	3.791	1.261
	0.339	3.528	2.968	1.458	4.225	1.271
	0.374	3.003	3.203	1.395	4.628	1.206
	0.417	2.449	3.456	1.349	5.004	1.243
	0.465	2.151	3.722	1.281	5.377	1.274
	0.522	1.890	3.996	1.236	5.785	1.314
	0.589	1.620	4.313	1.241	6.275	1.390
	0.667	1.451	4.652	1.220	6.803	1.440
	0.769	1.277	4.981	1.200	1.243	1.362
	0.884	1.147	5.311	1.271	1.382	1.458
	0.993	1.189	5.640	1.262	1.548	1.532
	1.091	1.309	5.932	1.321	1.734	1.604
	1.185	1.386	6.214	1.328	0.412	2.626
	1.268	1.359	6.502	1.379	0.436	2.441
	1.306	1.451	6.801	1.473	0.468	2.157
	1.454	1.533	7.130	1.514	0.296	4.178
	1.603	1.587	1.898	1.598	0.318	3.951
	1.766	1.621	2.126	1.601	0.343	3.461
	1.940	1.619	2.380	1.620	0.375	3.054
	2.128	1.634	2.653	1.511	0.416	2.584
	2.320	1.631	2.972	1.430	0.469	2.243
(b)	0.418	2.517	0.305	4.215	2.294	1.599
	0.532	1.875	0.334	3.608	2.665	1.527
	0.656	1.395	0.360	3.180	3.043	1.463
	0.729	1.255	0.394	2.785	3.373	1.371
	1.091	1.308	0.444	2.343	3.708	1.340
	1.234	1.350	0.507	2.042	4.045	1.298
	1.386	1.440	0.587	1.640	4.387	1.336
	1.540	1.541	0.678	1.323	4.735	1.301
	1.701	1.577	0.776	1.169	5.087	1.331
	1.873	1.609	0.872	1.103	5.458	1.364
	2.057	1.635	0.966	1.180	5.801	1.400
	2.256	1.611	1.090	1.334	6.145	1.479
	2.476	1.542	1.256	1.373	6.505	1.485
	0.312	3.870	1.453	1.449	6.894	1.577
	0.349	3.337	1.712	1.569		
	0.388	2.893	1.994	1.630		

0.3–7 K. The heat capacity of the adsorbed gas was determined from the difference between the heat capacities of the calorimeter system with and without adsorbed CH_3D. When the system has no large thermal anomaly, such as a Schottky anomaly, this difference may be very small, amounting in some cases to only a few percent of the total heat capacity even at low temperatures. Very high accuracy is then required. CH_3D, however, had large Schottky anomalies, the contribution to the total heat capacity of the system being at least 7% at 7 K and up to 95% at 0.3 K. The accuracy of the data for the two coverages, for which the heat capacities are given in Table IX, is mainly limited by thermal relaxation at lower temperatures and by the small contribution of the CH_3D to the overall heat capacity at higher temperatures. The result is an accuracy of about ± 2% over the whole temperature range.

On our Grafoil MAT 0.25 mmol g^{-1} corresponds to a monolayer as defined by the inflection point in the first step of the adsorption isotherm of CH_4 at 77 K.[5] The higher of the
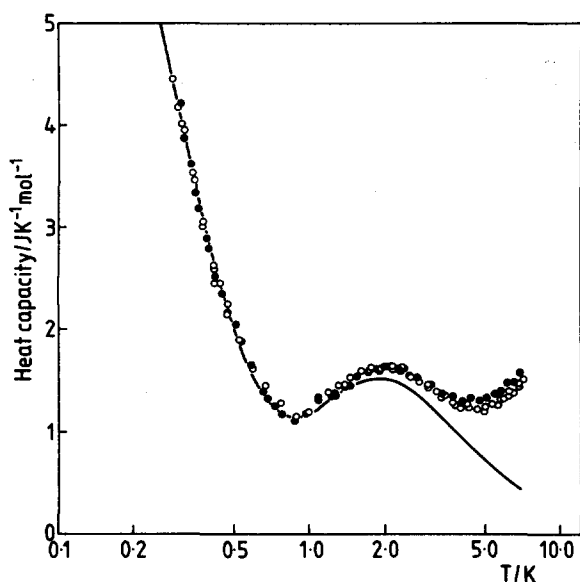
FIG. 6. The observed heat capacities of a layer of CH_3D at two different coverages 0.81 (●) and 0.94 (○). The continuous line is calculated for $\Delta a = -380\,\mu eV$ and the values of the energy levels corresponding to column (A) in Table X, but it is essentially unchanged for the values in column (B).

two amounts adsorbed, 3.014 mmol, therefore corresponds to a coverage of 0.94, and is exactly at the peak of the heat of adsorption for CH_4 at 64 K associated with the incommensurate solid/fluid phase transition.[5] This coverage might therefore exceed the maximum coverage for the commensurate structure. On the other hand, the lower amount adsorbed corresponds to a coverage of 0.81 and must be well within the commensurate region of the phase diagram. Despite the closeness of the higher coverage to the incommensurate phase boundary the two sets of measurements are practically indistinguishable below 3 K.

The heat capacity curve of Fig. 6 is dominated by the difference between the D-up and D-down states, i.e., by $\Delta a = a - a_4$, and is relatively insensitive to the finer details of the splittings within each set of levels. We therefore use the values of h and h_4 determined for CH_4[10] and the values of f and f_4 deduced by Maki[11] (see Sec. III) and attempt to fit the heat capacity data by adjustment of Δa. Maki gave two estimates for Δa of -46 and $-68\,\mu eV$. Neither reproduces the observed heat capacity. The best fit, shown as a continuous line in Fig. 6, is obtained for $\Delta a = -380 \pm 20\,\mu eV$, which means that the configuration with the C–D bond pointing towards the surface is much more stable than expected with respect to that with the C–D bond pointing upwards.

The agreement between calculated and observed curves is impressive below 1 K, where the vibrational heat capacity of the two-dimensional lattice is not significant. As can be seen in Fig. 6, the lattice contribution becomes significant above 1 K. We can extract the vibrational contribution by subtracting the fitted Schottky anomaly from the experimental values of the heat capacity. A plot of the resulting values of C/T^2 against T yielded $\beta = 17$ and 20

$mJ\ K^{-3}\ mol^{-1}$ for the 0.94 and 0.81 coverage samples, respectively, where β is the coefficient of the T^2 term in the lattice heat capacity. These values are comparable with those for other simple molecules on graphite.[21] The difference between the two is also reasonable because the layer is possibly incommensurate at a coverage of 0.94 and the lattice vibrations in the incommensurate phase would generally be expected to be shifted to higher frequencies relative to those of the commensurate phase.

V. INELASTIC NEUTRON SCATTERING SPECTRA

A. Experimental details

The adsorbent used was the partially recompressed exfoliated graphite Papyex (Le Carbone Lorraine). It had a surface area of 20 $m^2\ g^{-1}$ with a mosaic spread in the orientation of the graphite basal planes of about 30°. The Papyex was contained in an aluminum welded can and outgassed immediately before each experiment at 2×10^{-4} Pa and 350 °C. The dimensions of the can were chosen to suit each experiment. For the higher-energy-transfer experiments (IN5), the cans were cylindrical, 6 cm in diameter, and 1 cm thick, with the cross section of the cylinder in a plane perpendicular to the neutron beam. Each can contained about 25 g Papyex cut into 6-cm-diameter disks. The Papyex could therefore easily be oriented with respect to the momentum-transfer vector κ. For the IN10 experiments, the aluminum sample can was cylindrical with the cylinder axis perpendicular to the beam, the height and diameter of the cylinder being 4 cm. For experiments with κ parallel ($\kappa \parallel$) to the surface, the Papyex was in the form of disks lying in the scattering plane, thus giving a good definition of the direction of κ with respect to the surface. For experiments with κ perpendicular ($\kappa \perp$) to the surface, the definition of the direction of κ was less satisfactory because the Papyex sheets were now aligned perpendicular to the scattering planes so that they bisected the scattering angle. The analyzer–detector combination on IN10 covers quite a wide angular range so that the $\kappa \perp$ spectrum may be significantly contaminated (20%–30%) by parallel polarized transitions. The background scattering from the sample and container was recorded before volumetric dosing of the sample with CH_3D. Adsorption was carried out at around 80 K and then the sample cooled slowly to 4.2 K. The coverage quoted is based on the measured surface area of the Papyex used (21 $m^2\ g^{-1}$), a molecular area of 14.7 $Å^2$ (corresponding to the incommensurate phase), and a molar volume of the gas of 24.6 dm^3 at 300 K.

All the experiments were done at the Institut Laue-Langevin.[22] For energy transfers in the range 0–5 meV (0–40 cm^{-1}), the time-of-flight spectrometer IN5 was used with an incident wavelength of 10 Å and a resolution of 15 μeV. For lower energy transfers, the back-scattering spectrometer IN10 was used with an incident wavelength of 6.28 Å and a resolution of 1 μeV. In the IN5 spectrometer, sufficient detectors could be placed within a narrow range of angles to give a reasonable definition of the direction of κ with respect to the surface.
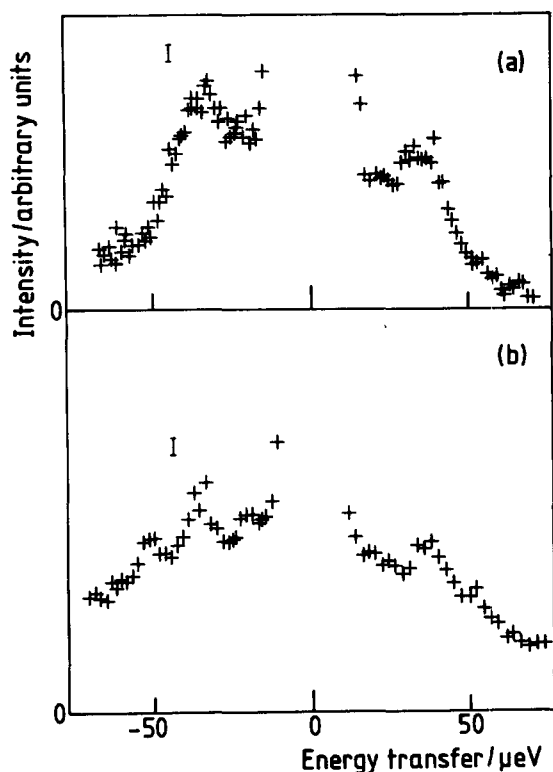
FIG. 7. Low resolution tunneling spectra of CH_3D on graphite after subtraction of the graphite background, (a) with κ parallel to the surface and (B) with κ perpendicular to the surface. $T = 4.2$ K and coverage $= 0.7$.

B. Results

The spectra of CH_3D adsorbed on Papyex at a coverage of 0.7 monlayer at 4.2 K are shown for κ parallel and perpendicular to the surface of the graphite in Figs. 7 and 8. Figure 7 shows the lower resolution spectra obtained on IN5 after subtraction of the graphite background and Fig. 8 shows higher resolution spectra in the energy transfer range 10–40 μeV with no background subtracted. The background from graphite in this region of energy transfer is known to be flat. However, the high level of background to features in the spectrum shows how difficult are experiments on the deuterated methanes. An unsuccessful attempt was made to measure spectra in the 0–10 μeV range. The resolution function of IN10 is Lorentzian in shape. This gives rise to a tail from the strong elastic scattering which, combined with a low signal from the CH_3D and significant broadening of several of the transitions, made it impossible to observe any transitions with certainty in this lower energy range.

In the lower resolution $\kappa\perp$ study [Fig. 7(b)], there is a weak peak in the region 15–20 μeV, at too low an energy transfer to be accurately resolved, a strong peak at about 37 μeV whose width suggests that it may consist of two overlapping transitions, and a weak peak at 53 μeV. The higher resolution study [Fig. 8(b)] shows that the position of the inner peak is 16 μeV and that there is a definite shoulder on the peak centered at 37 μeV. In the lower resolution $\kappa\|$ study, there is an intense envelope of scattering centered at
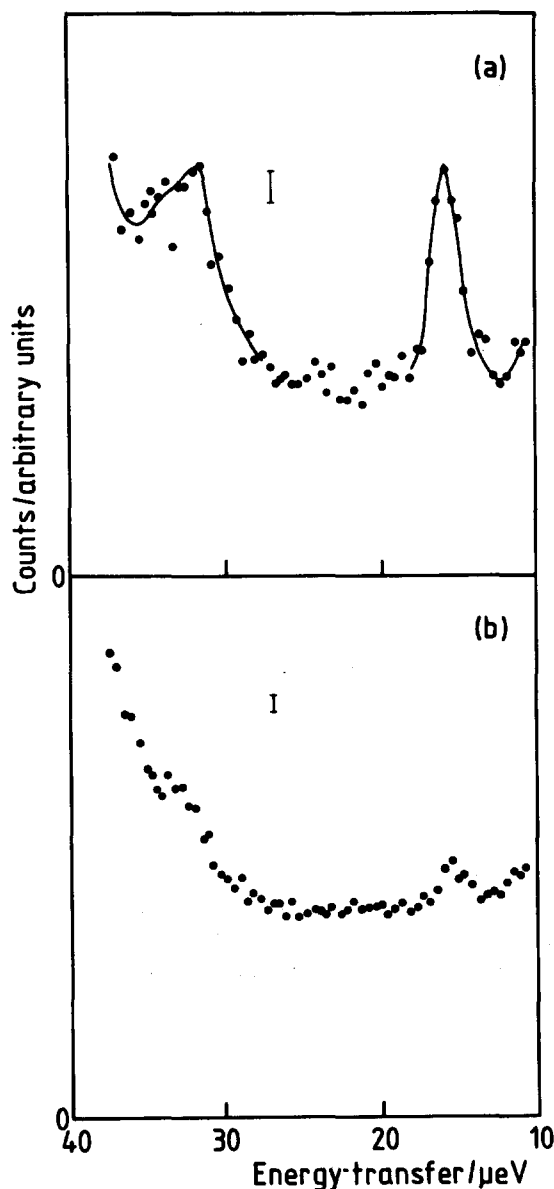
FIG. 8. High resolution tunneling spectra of CH_3D on graphite. (a) With κ parallel to the surface and (b) with κ perpendicular to the surface. $T = 4.2$ K and coverage $= 0.7$.

34 μeV and a noticeable broadening of the elastic peak compared with the $\kappa\perp$ spectrum, suggesting that there is at least one intense transition falling within the resolution of the instrument. This transition is observed clearly in the IN10 spectrum [Fig. 8(a)], where there is an intense line at 16 μeV. The only other feature of this spectrum is a strong line at 31–32 μeV, broadened by another peak or peaks at higher energy transfers.

The above statements summarize all the observations, which we now compare with the predicted spectra of Fig. 5. To help make the arguments for our assignment more clear, we also tabulate the predicted energies of the transitions in column 3 (energy (a)) of Table X using the values of h, h_4, f, and f_4 given in Sec. III.

There is certainly no transition above 53 μeV when κ is perpendicular to the surface the outer line in the low resolu-

TABLE X. Energies of tunneling transitions of CH_3D on graphite. Energy(a) are values determined from values of the matrix elements given by Maki (Ref. 11) and energy(b) are the observed values.

Assignment	|Energy|	Energy(a)	Energy(b) (μeV)	Appearance
(A)$\kappa\|$				
$A_1^{(u)}-E_3^{(u)}$	$3h_4$	24	31.5	Sharp,strong
A_1-E_3	$3h + 3f + 3f_4$	59.7	59.7	Sharp,weak
A_1-E_1	$3h + 3f$	54	53.1	Sharp,weak
A_1-E_4	$3h + 3f_4$	49.7	50.1	Sharp,strong
E_2-E_3	$3h$	42	43.5	Broad,strong
E_2-E_1	$3h - 3f_4$	36.3	36.9	Broad,strong
E_2-E_4	$3h - 3f$	30	33.9	Broad,medium
A_1-E_2	$3f + 3f_4$	17.7	16.2	Sharp,medium
E_3-E_4	$3f$	12	9.6	Broad,weak
E_1-E_3	$3f_4$	5.7	6.6	Broad,strong
E_4-E_1	$3f - 3f_4$	6.3	3.0	Broad,weak
(B)$\kappa\perp$				
A_1-E_1	$3h + 3f$	54	53.1	Sharp
E_2-E_3	$3h$	42	43.5	Broad
E_2-E_4	$3h - 3f$	30	33.9	Broad
E_4-E_3	$3f$	12	9.6	Broad

tion spectrum must therefore be assigned to the $A_1^{(d)} - E_1$ transition such that

$$3h + 3f = -53 \ \mu\text{eV}. \qquad (5.1)$$

It would then seem natural to assign the line at 16μeV in the $\kappa\perp$ spectrum to the transition $E_4 - E_3^{(d)}$. However, this leads to an assignment inconsistent with other features in the spectra. This is because such an assignment would make $f = -5.3 \mu$eV. From Eq. (5.1), h would then be -12.3 μeV and hence the transition $E_2 - E_4$ would be predicted to occur at 21μeV, where no transition is observed. The great intensity of the line at 16μeV in the $\kappa\|$ spectrum suggests that the 16μeV line in $\kappa\perp$ is the same transition which, although polarized parallel to the surface, is observed because of imperfect orientation of κ with respect to the surface. As explained in the experimental section, the high-resolution $\kappa\perp$ spectrum is expected to be contaminated by 20%–30% of the $\kappa\|$ spectrum, which would account well for the observed intensity. We therefore conclude that there are no genuine $\kappa\perp$ transitions in the range 10–30 μeV and that $|3f| < 10 \mu$eV, as anticipated. The best assignment of the remaining features of the $\kappa\perp$ spectrum is to take the shoulder at 34μeV to be the E_2-E_4 transition, which gives

$$3h - 3f = -34 \ \mu\text{eV}. \qquad (5.2)$$

The combination of Eqs. (5.1) and (5.2) then gives $h = -14.5$ and $f = -3.2 \mu$eV. The $E_2 - E_3^{(d)}$ and $E_4 - E_3^{(d)}$ transitions are then predicted to lie at 43.5 and 9.6 μeV, respectively. Clough[23] has suggested that E states may be substantially broader than A states and therefore three of the four transitions in the $\kappa\perp$ spectrum may be broad. The E_2-E_4 and $E_4-E_3^{(d)}$ transitions would then not be expected to be resolved and their center of gravity should lie at about 39 μeV, close to the maximum observed in the IN5 spectrum. There is also an additional line broadening because the molecule sits in a potential which varies according to the configuration of the surroundings (there are different orien-

tations of the C–D bonds for each of the six molecules surrounding the "test" molecule).

The broadening effect undoubtedly confuses the assignment of the $\kappa\|$ spectra, for which 11 lines are predicted, but only two really distinct features are observed. Comparison of Figs. 5(a) and 8(a) makes the only sensible assignments of the peaks at 16 and 31.5 μeV, the $A_1^{(d)}-E_2$ and $A_1^{(u)}-E_3^{(u)}$ transitions, respectively. This gives

$$3f + 3f_4 = -16 \mu\text{eV}, \qquad (5.3)$$

$$3h_4 = -31.5 \mu\text{eV} \qquad (5.4)$$

making $h_4 = -10.5 \mu$eV and $f_4 = -2.2 \mu$eV. Since h and f have been independently determined from the $\kappa\perp$ spectra, the positions of all the lines in the $\kappa\|$ spectrum are now fixed and are given in column 4 [energy (b)] of Table X together with qualitative descriptions of their intensities and expected widths. The qualitative features of the IN10 spectrum are well reproduced by this scheme. Thus there is no scattering between 16 and 31.5 μeV and the envelope of scattering at the high energy edge of the window is attributed to a combination of the broad E_2-E_4 and E_2-E_1 transitions with the tail of the E_2-E_3 transition. That the three most intense lines in the spectrum (of approximately equal intensity) are thereby predicted to be at 31.5, 37, and 43.5 μeV, also agrees well with the main feature of the IN5 spectrum. There are two features that do not accord well with the IN5 spectrum. Firstly, there is no sign of the expected line at 50 μeV. Secondly, the relative intensities of the two assigned transitions are not correct; theoretically the D-up state transition should be 1.8 times as intense, whereas experimentally they are of comparable intensity. A further reservation about the assignment is the failure to observe any transitions in the energy range 0–10 μeV. Given the limitations of the experiment in this range, as outlined in Sec. V A above, this may not be surprising, especially for the $\kappa\|$ experiment where three equally spaced, broad transitions fall within the energy

window. With these reservations, we obtain the following values for the parameters characterizing the ground librational state of CH_3D adsorbed on graphite:

$\Delta a = -380 \mu eV$; $h = -14.5 \mu eV$; $f = -3.2 \mu eV$;

$h_4 = -10.5 \mu eV$; $f_4 = -2.2 \mu eV$.

The alterations in the values of h, f, h_4, and f_4 were found to have no effect on the value of Δa required to fit the heat capacity curve. The final energy level scheme is shown in Fig. 9.

VI. BARRIERS TO ROTATION

Maki, in his Fig. 1, shows how the overlap matrix elements are affected by isotopic substitution for a tetrahedral potential. Since the rotational potential for methane on graphite is quite close to tetrahedral, we may use this diagram to compare our values for h and f (or h_4 and f_4). Thus, if the orientational potential about one of the three equivalent C–H bonds contains just the lowest Fourier component, the observed value of $-14.5 \mu eV$ for h should become a value of $-4.1 \mu eV$ for f. The observed value for f is, however, only $-3.2 \mu eV$ and therefore there must be some contribution from higher Fourier components. We can estimate what effect this may have on the derived value of the barrier height as follows: Humes *et al.*[24] have calculated the matrix elements h and h_4 as a function of the two barrier heights. For CH_4, the observed value of h was $-14 \mu eV$ corresponding to a barrier height for rotation about the nonunique axis of 172 cm^{-1}. For CH_3D, h is observed to be $-14.5 \mu eV$ which corresponds to a barrier height of 169 cm^{-1}. The barrier height can be calculated independently from f. The observed value of f is $-3.2 \mu eV$, which corresponds to a value of h of $-10 \mu eV$ and a barrier of 180 cm^{-1}. Thus, although there are quite large differences in the various values of the overlap matrix elements, the values obtained for the barrier height have a narrow spread. This is because of the great sensitivity of tunneling splitting to the barrier height. However, it is evident from the discrepancies that the shape of the potential is not well described by a single Fourier component. Unfortunately, it is too complicated to analyze this quantitatively using the pocket-state treatment. However, it is possible to make an estimate of the contributions of higher Fourier components to the potential by using exact results from the one-dimensional problem.

Exact values for the tunneling splitting for a potential of the form

$$V = \tfrac{1}{2}A(1 - \cos 3\alpha)$$

can be obtained from tables of solutions for the Mathieu equation.[25] Herschbach has given additional tables which allow the effects of the next higher Fourier component (in $\cos 6\alpha$) to be included.[26] We note that in the pocket-state treatment, the tunneling splitting is $3h$, where h is the overlap matrix element. Owing to the different shape of the pocket-state wave functions in one and three dimensions values of h in the two cases are different for a given barrier height. For example, a value of $-14.5 \mu eV$ for h requires a barrier height of 170 cm^{-1} in the 3D case, but only 130 cm^{-1} in the
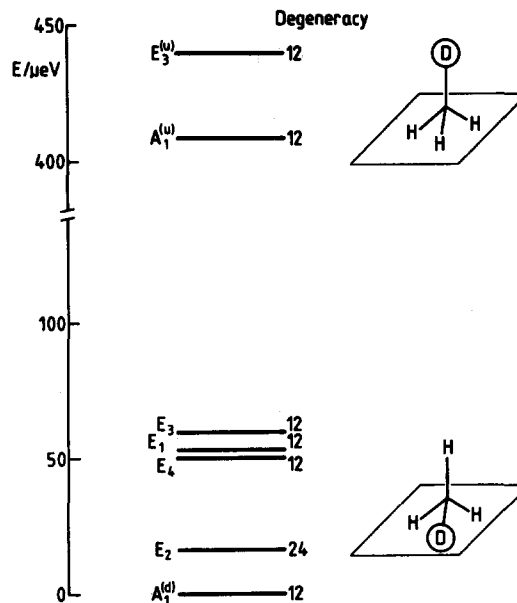

FIG. 9. Observed energy levels for CH_3D adsorbed on exfoliated graphite. The degeneracies of the levels, used for modeling the heat capacity, are also included.

1D case. Thus we have to be careful how we make the comparison between 1D and 3D.

In the 3D case, the observed values of h and f are -14.5 and $-3.2 \mu eV$, respectively, in the ratio 4.53:1. From Fig. 1 of Maki,[11] a value of h of -14.5 corresponds to a value of f of -4.1 and a ratio of 3.53, or a value of f of -3.2 corresponds to a value of h of -12 and a ratio of 3.75. The mean of these two theoretical values is 3.6 and it must be increased by a factor of 1.25 to match the observed ratio of 4.5. In the 1D case, corresponding values of h and f are -14.5 and -5.1 or -10 and $-3.2 \mu eV$, and the average ratio between them is 3.0. The main effect of the inclusion of the next higher Fourier component, the sixfold term, in the 1D case is to alter this ratio. If we now increase the proportion of the sixfold potential to change the ratio to 3.0×1.25 while keeping the overall scale of the potential at a value that keeps h at about $-12 \mu eV$ (approximately the average of the two alternative values), we find that the ratio V_6/V_3 is $+0.35$. This represents a substantial change in the shape of the potential. However, it corresponds to only a small change in the barrier height. Thus, in one dimension, the barrier height of a pure V_3 potential required to make $h = -12 \mu eV$ is 166 cm^{-1}. In the two component potential which gives the same value of h, V_3 is 118 and V_6 41 cm^{-1}, giving a total barrier of 159 cm^{-1}, only 4% lower. It is not unreasonable to suppose that the results from the 1D case scale to the 3D case. We then conclude that higher Fourier components make a substantial contribution to the rotational potential, but that the overall barrier to rotation about one of the nonunique C–H bonds of 172 cm^{-1} is accurate to better than 5%.

A similar treatment may be given for rotation about the unique axis. Thus the observed values of h_4 and f_4 are -10.5 and $-2.2 \mu eV$, respectively. If h_4 is -10.5, the value of f_4 expected from Maki's Fig. 1 is $-2.7 \mu eV$. The discrepancy

between the observed and expected ratios for h_4/f_4 is 1.23, very similar to the discrepancy for h and f. Thus the identical argument as given in the previous paragraph suggests that for rotation about the unique C–H bond the proportion of the sixfold contribution is about one-third and that it is in phase with the threefold contribution. However, once again, in order to maintain the magnitude of h_4 at 10.5 μeV, the height of the barrier must remain close to the value for a simple threefold potential.

The overall result of the measurements on CH_3D then gives the rather satisfactory result that the values of the barrier heights obtained by Smalley *et al.*[10] are not drastically affected by those authors' use of the approximation of a simple threefold potential about each of the two directions of rotation. However, there are a number of smaller discrepancies between the results from different systems which suggest that further analysis at a level that does not seem possible at present could yield yet more precise information about the rotation potential. We now outline some of these discrepancies.

At first sight the values of h and h_4 for CH_3D and CH_4 do not agree very well. $|h|$ is only about 3% larger for CH_3D, but $|h_4|$ is about 30% larger. However, the sensitivity of the tunneling frequencies to the potential is so high that the consequent changes in the barriers are relatively small. Thus the two barriers for CH_4 are 202 and 172 cm^{-1} and the corresponding values deduced from h and h_4 for CH_3D are 190 and 170 cm^{-1} $\pm$ 2%. Differences are also observed when the coverage is varied between 0.2 and 0.9, the layer remaining in its commensurate phase,[24] when the adsorbent is changed from exfoliated graphite to graphitized carbon black,[10] and when CH_4 is surrounded by CD_4.[24] In the latter case, $|h_4|$ decreases from 8 to 5.9 μeV and $|h|$ from 14 to 13.2 μeV, corresponding to an increase of 8% in the unique barrier and a decrease of 1% in the nonunique one on changing the surroundings of a CH_4 molecule from CH_4 to predominantly CD_4. The differences in the tunneling splittings on graphitized carbon black are strikingly demonstrated by the spectrum shown by Maki,[11] where there are lines in the region of 25 μeV, which do not appear in either of the spectra shown in Fig. 8. They can also be observed for CH_4 itself by comparing the results from Smalley *et al.*[10] using Papyex and those of Newbery *et al.*[27] using the graphitized carbon blacks Vulcan III and Sterling FT. All these changes may have their origin either in a change in the average potential, perhaps resulting from differences in the zero point motion of the whole layer, or in weak coupling between the motions of adjacent molecules. The latter effect would cause the spectrum to depend on more parameters than we have used to fit the spectrum of CH_3D and could be the explanation of some of the uncertain features of our assignment.

ACKNOWLEDGMENT

APPENDIX

The decrease in tunneling frequency resulting from asymmetry in a double minimum potential depends on the barrier height V_0 and on the difference in the potential minima ΔV. In the limit of small asymmetry and small tunneling frequency (which we may assume to be the case for CH_3D on graphite), it can be shown that[18]

$$\nu_t = \nu_t^0 \left(\frac{2\Delta E}{[(\Delta E)^2 + 4(\Delta V)^2]^{1/2}} \right), \tag{A1}$$

where ν_t is the tunneling frequency, ν_t^0 is the tunneling frequency in the limiting symmetric potential, $2\Delta E = h\nu_t^0$, and ΔV is the difference in energy of the two potential minima. We note in passing that Eq. (A1) cannot be correct because in the limiting case of $\Delta V = 0 \nu_t = 2\nu_t^0$. However, this will not be important in our order of magnitude calculation below.

ΔV is in our case the energy difference Δa between the two types of pocket state, which we know to be -380μeV. The off-diagonal elements of the Hamiltonian give directly the tunneling energies $h\nu_t$ between the pocket states. Thus, for the symmetric potential $h\nu_t^0 = h_5$, i.e., $\Delta E = 2.0 \mu$eV. Using these values in Eq. (A1), we obtain

$$h_2 = -5 \times 10^{-3} \mu\text{eV}.$$

This value makes the matrix element h_2 three orders of magnitude smaller than the other four threefold elements. The perturbation between eigenstates containing only $\phi^{(u)}$s and those containing only $\phi^{(d)}$s is given by

$$\Delta E = \frac{|\langle \psi^{(u)}|H|\psi^{(d)}\rangle|^2}{E_\psi^{(u)} - E_\psi^{(d)}} + \text{higher terms}$$

which will be of the order of

$$|h_2|^2/\Delta a \simeq -10^{-7} \mu\text{eV}.$$

This is an entirely negligible perturbation.

[1] E. S. Severin and D. J. Tildesley, Mol. Phys. **41**, 1401 (1980).

[2] J. M. Phillips, Phys. Rev. B **29**, 4821 (1984).

[3] K. Maki and M. L. Klein, J. Chem. Phys. **71**, 1488 (1981).

[4] A. Thomy and X. Duval, J. Chim. Phys. **67**, 286 (1970).

[5] I. Inaba, Y. Koga, and J. A. Morrison, J. Chem. Soc. Faraday Trans. II **82**, 1635 (1986).

[6] H. K. Kim and M. H. W. Chan, Phys. Rev. Lett. **53**, 170 (1984).

[7] P. Vora, S. K. Sinha, and R. K. Crawford, Phys. Rev. Lett. **43**, 704 (1979).

[8] T. Rayment, R. K. Thomas, G. Bomchil, and J. W. White, Mol. Phys. **43**, 601 (1981).

[9] G. Bomchil, A. Hüller, T. Rayment, S. J. Roser, M. V. Smalley, R. K. Thomas, and J. W. White, Philos. Trans. R. Soc. B **290**, 537 (1980).

[10] M. V. Smalley, A. Hüller, R. K. Thomas, and J. W. White, Mol. Phys. **44**, 533 (1981).

[11] K. Maki, J. Chem. Phys. **74**, 2049 (1981).

[12] A. Inaba and J. A. Morrison, Bull. Chem. Soc. Jpn. **61**, 25 (1988).

[13] A. Hüller, Phys. Rev. **16**, 1844 (1977).

[14] A. Hüller and J. Raich, J. Chem. Phys. **71**, 3851 (1979).

[15] M. V. Smalley and P. C. Ball (to be published).

[16] R. L. Somorjai and D. F. Hornig, J. Chem. Phys. **36**, 1980 (1962).

[17] J. Brickmann and H. Zimmerman, J. Chem. Phys. **50**, 1608 (1969).

[18] M. D. Harmony, Chem. Soc. Rev. **1**, 211 (1972).

[19] Y. Ozaki, Y. Kataoka, and T. Yamamoto, J. Chem. Phys. **73**, 3442 (1980).

[20] P. R. Norton, J. Chromatographic Soc. **8**, 411 (1970).

[21]A. Inaba and H. Chihara (to be published).

[22]*Neutron Facilities at the High Flux Reactor*, edited by H. Blank and B. Maier (Institut Laue-Langevin, Grenoble, 1986).

[23]S. Clough, A. Heidemann, and K. Kraxenburger, Phys. Rev. Lett. **42**, 1298 (1979).

[24]R. P. Humes, M. V. Smalley, T. Rayment, and R. K. Thomas, Can. J. Chem. **66**, 557 (1988).

[25]D. R. Herschbach, *Tables Relating to Mathieu Functions* (Columbia University, New York, 1951).

[26]D. R. Herschbach, J. Chem. Phys. **31**, 91 (1959).

[27]M. W. Newbery, T. Rayment, M. V. Smalley, R. K. Thomas, and J. W. White, Chem. Phys. Lett. **59**, 461 (1978).